PTEP

Prog. Theor. Exp. Phys. **2016**, 053E01 (18 pages)
DOI: 10.1093/ptep/ptw043

Synergy between ground- and space-based gravitational-wave detectors for estimation of binary coalescence parameters

Remya Nair[1], Sanjay Jhingan[2,*], and Takahiro Tanaka[3]

[1] *The Inter-University Centre for Astronomy and Astrophysics, Pune-411007, India*
[2] *Centre for Theoretical Physics, Jamia Millia Islamia, New Delhi-110025, India and iCLA, Yamanashi Gakuin University, 2-4-5, Sakaori, Kofu-City, Yamanashi 400-8575, Japan*
[3] *Yukawa Institute for Theoretical Physics, Kyoto University, Kyoto 606-8502, Japan and Department of Physics, Kyoto University, Kyoto 606-8502, Japan*
*E-mail: sanjay.jhingan@gmail.com

Received March 5, 2016; Accepted March 17, 2016; Published May 24, 2016

We study the advantages of the coexistence of future ground- and space-based gravitational-wave detectors in estimating the parameters of a binary coalescence. Space measurements will act as a precursor to ground measurements. Also, since space measurements will provide much better localization information on the source, they will aid electromagnetic follow-up of the source and hence increase the probability of finding an electromagnetic counterpart of the gravitational-wave event. Using the post-Newtonian waveform for the inspiral of nonspinning neutron star–black hole binaries in circular orbits, we analyze how estimates for the chirp mass, the symmetric mass ratio, and the time and phase at coalescence are improved by combining the data from different space–ground detector pairs. Since the gravitational waves produced by binary coalescence also provide a suitable domain where we can investigate strong field gravity, we also study the deviations from general relativity using the parameterized post-Einsteinian framework. As an example, focusing on the Einstein telescope and DECIGO pair, we demonstrate that there exists a sweet-spot range of sensitivity in the pre-DECIGO period where the best enhancement due to the synergy effect can be obtained for estimates of the post-Newtonian waveform parameters. Similar results are obtained for the parameter that characterizes deviation from general relativity.

Subject Index E02, F31

1. Introduction

Two unique predictions of general relativity (GR), black holes (BHs) and gravitational waves (GWs), are now confirmed [1]. In a beautiful coincidence, this glorious journey for their search ended by simultaneous observation of a transient gravitational-wave signal in the two advanced LIGO detectors, in the centennial year of GR, on 14 September 2015. This observation of the inspiral, merger, and resulting ringdown of a binary black hole system (GW150914) matches the waveform predicted by GR with a significance greater than 5σ. This is the first direct detection of gravitational waves, and the first observation of a binary black hole merger has set the course for a new era in observational astronomy and astrophysics. The successful run that GR has enjoyed so far [2] does not end with the discovery of GWs. In fact, this discovery will now boost research in new directions, such as the search for super-massive BHs at the center of galaxies [3], stochastic GW background, similar to the

cosmic microwave background [4] etc. The incredible agreement of the GW signal with GR puts a strong constraint on the prospect of discovering that GR may need modifications in the strong field regime. This has been one of the motivations for the development of alternative theories of gravity. GW signals will provide a testing ground for these theories and a wide range of tests of GR have already been proposed. Tests that use GWs coming from compact binary coalescence include those proposed in Refs. [8–14].

GW150914 is an immaculate and super-loud signal (matched filtering signal-to-noise ratio of 23). The signal originated from a binary black hole system with component masses $36^{+5}_{-4}M_{\odot}$ and $29^{+4}_{-4}M_{\odot}$ at a redshift $0.09^{+0.03}_{-0.04}$. The two black holes merged to form a $62^{+4}_{-4}M_{\odot}$ mass BH with spin $0.67^{+0.05}_{-0.07}$ [15]. The final BH is more massive than any found in the stellar BH mass range. Although the first detection of GW turned out to be from a black hole binary, coalescing binaries composed of neutron stars (NSs) and BHs are expected to be amongst the most likely sources for GW signals to be observed by ground-based interferometric detectors. The post-Newtonian (PN) formalism has been used to model the inspiral part of the binary evolution within GR. In the PN formalism, physical quantities of interest such as the conserved energy, flux etc. can be written as expansions in the small parameter (v/c), where v is the characteristic speed of the binary system and c is the speed of light [16]. In the standard convention, $O((v/c)^n)$ corrections counting from the leading order are referred to as $(n/2)$PN-order terms. For the derivation of various PN expansion terms in the amplitude and the phase of the GW signal from inspiralling binaries, please see Refs. [16–20] and references therein. These inspiralling binaries are suitable for studying the strong field regime since the orbital velocities in these systems can go as high as $v/c \sim O(1)(\sim 0.5)$, and therefore higher-order PN corrections are relevant. The standard data analysis techniques used for the detection and characterization of GW signals originating from compact binaries depend on the availability of GW templates. Accurate templates are necessary to identify the weak GW signal buried in noise. However, in order to carry out tests of GR, it is impractical to make accurate templates for all possible alternative theories of gravity. A more feasible way of carrying out such tests is to adopt general non-GR templates to model the signals. Arun et al. proposed such templates in which the expansion coefficients of the frequency-domain GW phase (see Eq. (3)) are treated as fitting parameters [11]. In GR, each of these coefficients are specified by the masses and spins of the compact objects constituting the binary. In principle, these relations could be completely different in some alternative theory of gravity and may even involve other parameters.

Yunes and Pretorius developed the parameterized post-Einsteinian (ppE) framework, which accommodates a wider range of deviations to the amplitude and phase of the waveform [12]. Similar to the parameterized post-Newtonian framework, the authors introduced ppE parameters, but, instead of parameterizing the metric tensor, the GW waveform was parameterized using a generic template family (see Sect. 2.2). This family can accommodate the inspiral phase of most of the known alternative theories of gravity with appropriate choices of the parameters. Cornish et al. applied the ppE approach to simulated data to determine the level at which departures from GR can be detected, and also analyzed the bias introduced in the extraction of the model parameters due to the assumption of the incorrect theory [13].

In this work, we study the synergy between the ground- and space-based GW detectors in estimating the parameters of the inspiralling binaries, to investigate whether there is any gain in combining measurements from two detectors. For this purpose we use the PN template for the inspiral of binaries, and we also use the ppE framework proposed by Yunes and Pretorius [12]. We consider a future space-based detector, DECIGO, and two future ground-based detectors, advanced LIGO

and ET. As representative test cases, we consider two binary systems, a $1.4\,M_\odot + 10\,M_\odot$ binary and a $1.4\,M_\odot + 100\,M_\odot$ binary, where $M_\odot$ is the solar mass. Within the PN framework, we study the synergy effect in detail for the chirp mass, the symmetric mass ratio, and the time and phase at coalescence. In the ppE framework, we explore the error estimation of the ppE parameter characterizing deviation from GR. Note that the study of orbital motion of the space-based detectors is important since it helps in source localization through Doppler modulation of the phase. However, we ignore this effect in the present study because the purpose of the present paper is just to show the order of magnitude of the nontrivial synergy effect. We will consider the complete study with orbital motion and source localization in a future publication.

The plan of the paper is as follows: in the next section we briefly describe the waveforms used in this analysis (Sects. 2.1, 2.2), the noise curves for the different detectors are given in Sect. 2.3, the methodology for error estimation is mentioned in Sect. 2.4, and we summarize our results in Sect. 3.

2. Methodology

2.1. *PN formalism*

We begin by writing the frequency-domain GW signal $h(f)$, for nonspinning inspiralling binaries in circular orbits (under the stationary phase approximation) [21]. Moreover, we use the *restricted PN waveforms*, which keep the higher-order terms in phase but only take the leading-order terms for the amplitude [22]. In the matched filtering analysis used for parameter estimation, the correlation of two waveforms is more sensitive to the deviation in phase than the deviation in amplitude. This is, however, not true for binaries with misaligned spins, where the amplitude modulation on a precession timescale is also important to determine the spin parameters [23]. Since such a modulation helps to resolve the degeneracy between spins and the other parameters, it is partly justified to consider nonspinning binaries to give approximate errors in the estimation of the other parameters. Hence, we consider only the leading-order term in the amplitude, while the phase terms are taken up to 3.5PN order. The expression for $h(f)$ reads:

$$h(f) = \mathcal{A}_{\rm GR} f^{-7/6} \exp(i\psi_{\rm GR}(f) + i\pi/4), \tag{1}$$

where the Fourier amplitude $\mathcal{A}_{\rm GR}$ is given by

$$\mathcal{A}_{\rm GR} = \frac{\mathcal{C}}{D\pi^{2/3}}\sqrt{\frac{5\nu}{24}}M^{5/6}, \tag{2}$$

and the phase $\psi_{\rm GR}(f)$ is given by

$$\psi_{\rm GR}(f) = 2\pi f t_c + \phi_c + \frac{3}{128\nu}\sum_{k=0}^{7}\alpha_k(\pi M f)^{(k-5)/3}, \tag{3}$$

where $\mathcal{C}$ is an $O(1)$ dimensionless geometric factor that depends on the relative orientation of the binary and the detector (average over all orientations $\bar{\mathcal{C}} = 2/5$). ν is the symmetric mass ratio defined as $\nu \equiv m_1 m_2/(m_1+m_2)^2$, where m_1 and m_2 are component masses of the binary system. M is the total mass of the binary $(m_1 + m_2)$, D is the luminosity distance to the binary, and t_c and ϕ_c are the time and phase at coalescence, respectively. The coefficients α_k are given below. For the purposes of this paper, the explicit expression for $\mathcal{C}$ is not necessary, as we also neglect the effects of the orbital motion of the space antenna. Note that terms with exponent $k = n$ are $(n/2)$ PN-order terms. The expressions for the amplitude and the phase are often also expressed in terms of the chirp

mass $\mathcal{M} = \nu^{3/5} M$ as

$$\mathcal{A}_{\rm GR} = \frac{C}{D\pi^{2/3}}\sqrt{\frac{5}{24}}\mathcal{M}^{5/6}, \tag{4}$$

and

$$\psi_{\rm GR}(f) = 2\pi f t_c + \phi_c + \frac{3}{128\nu}\sum_{k=0}^{7}\alpha_k\left(\frac{\pi\mathcal{M}f}{\nu^{3/5}}\right)^{(k-5)/3}. \tag{5}$$

The values of the coefficients appearing in (5) are as follows [21]:

$$\begin{aligned}
&\alpha_0 = 1, \quad \alpha_1 = 0, \quad \alpha_2 = \frac{3715}{756} + \frac{55}{9}\nu,\\
&\alpha_3 = -16\pi, \quad \alpha_4 = \frac{15\,293\,365}{508\,032} + \frac{27\,145}{504}\nu + \frac{3085}{72}\nu^2,\\
&\alpha_5 = \pi\left(\frac{38\,645}{756} - \frac{65}{9}\nu\right)\left[1 + \ln\left(6^{3/2}\pi M f\right)\right],\\
&\alpha_6 = \frac{11\,583\,231\,236\,531}{4694\,215\,680} - \frac{640}{3}\pi^2 - \frac{6848}{21}\gamma + \left(-\frac{15\,737\,765\,635}{3048\,192} + \frac{2255}{12}\pi^2\right)\nu\\
&\qquad + \frac{76\,055}{1728}\nu^2 - \frac{127\,825}{1296}\nu^3 - \frac{6848}{63}\ln(64\pi M f),\\
&\alpha_7 = \pi\left(\frac{77\,096\,675}{254\,016} + \frac{378\,515}{1512}\nu - \frac{74\,045}{756}\nu^2\right).
\end{aligned} \tag{6}$$

Note that we will also study a high-mass-ratio binary ($1.4\,M_\odot + 100\,M_\odot$) and it is unclear whether the restricted PN waveforms are a good choice for such binaries. One can replace them with a more appropriate template if one becomes available. However, we believe that this replacement may not affect the assessment of the synergy effect. In the next subsection, we briefly describe the ppE formalism.

2.2. *ppE formalism*

One of the most important outcomes of GW detection would be placing bounds on alternative theories of gravity [24,25]. Several such theories have been proposed to explain the observed late time acceleration of the Universe. Within the framework of GR, late time acceleration can be explained by invoking either the cosmological constant or by assuming the existence of some exotic matter fields. However, even the cosmological constant, which seems the most natural candidate, is difficult to accommodate within the standard model of particle physics, without appealing to the anthropic argument. An alternative approach is to realize classical GR as a low-energy limit of some more fundamental theory. In this case, one might expect nontrivial modifications to GR (e.g., nonminimally coupled dilatons etc.).

For studying the modification to GR using a parameterized approach, we follow the ppE formalism proposed by Yunes and Pretorius [12]. In this framework, modifications to the frequency-domain GW signal $h(f)$ from the inspiralling binary (1) enter through corrections to the Fourier amplitude and phase:

$$\begin{aligned}
\mathcal{A} &= \left(1 + \sum_i c_i(\pi\mathcal{M}f)^{a_i}\right)\mathcal{A}_{\rm GR}(f),\\
\psi(f) &= \psi_{\rm GR}(f) + \sum_i \beta_i(\pi\mathcal{M}f)^{b_i}.
\end{aligned} \tag{7}$$

Here $\mathcal{A}_{\rm GR}(f)$ and $\psi_{\rm GR}(f)$ are given by Eqs. (2) and (3) (the standard GR expressions), respectively. The corrections to these GR expressions are characterized by the amplitude parameters c_i and a_i and the phase parameters β_i and b_i. The coefficients c_i and β_i, in general, depend on the physical parameters of the binary. For the reason mentioned in the previous subsection, in the present analysis we concentrate on the modification in phase only. Therefore, we assume $\mathcal{A}(f) = \mathcal{A}_{\rm GR}(f)$ (i.e., $c_i = 0$ for all i). As a further simplification, we incorporate only the leading-order corrections to the phase:

$$\mathcal{A} = \mathcal{A}_{\rm GR}(f),$$
$$\psi(f) = \psi_{\rm GR}(f) + \beta(\pi\mathcal{M}f)^b. \tag{8}$$

Note that templates like those given in (7) are intrinsically non-unique, since a finite set of parameters cannot represent an infinite space of alternative theory templates. However, it involves the smallest number of ppE parameters that are necessary to reproduce (leading-order) corrections to the GW response function from almost all the known alternative theories of gravity [12]. For example, for the choice (c_i, a, β_i, b)=$(0, a, \beta_{\rm BD}, -7/3)$, it reduces to the Brans–Dicke theory, with $\beta_{\rm BD}$ related to a coupling parameter of the theory. For other modified theories and related parameter values, please refer to Ref. [12]. In the next section we discuss the noise curves of the various detectors examined in this paper.

2.3. *Noise curves*

The output of a GW detector, $s(t)$, is composed of two parts: the GW signal $h(t)$ and the detector noise $n(t)$, $s(t) = h(t) + n(t)$. For simplicity, we assume that the detector noise is stationary and Gaussian, i.e., the probability distribution of noise is given as $P(\tilde{n}) \propto \exp\left(-\left|\tilde{n}\right|^2/2\sigma^2\right)$, where the tilde denotes a Fourier transform, noise is assumed to have zero mean $\langle\tilde{n}\rangle = 0$, and σ^2 is the noise variance $\langle|\tilde{n}^2|\rangle = \sigma^2$. The angular brackets $\langle\rangle$ denote averaging over different noise realizations. Stationarity implies that the different Fourier components of the noise are uncorrelated, and hence the one-sided noise power spectral density $S_n(f)$ can be defined by

$$\langle\tilde{n}(f)\tilde{n}(f')\rangle = \tfrac{1}{2}\delta(f - f')S_n(f).$$

A commonly used quantity to describe the sensitivity of a GW detector is the square root of its power spectral density in units of $\mathrm{Hz}^{-1/2}$. The noise spectral densities of all the detectors used in this work are described in the following subsections.

2.3.1. *Future space-based detector*

– DECIGO: The Deci-hertz Interferometer Gravitational Wave Observatory (DECIGO) is a future plan of a space mission proposed by Seto et al. [27] (the Big Bang Observer is a similar plan [26]). The objective is to detect GWs in the frequency range $f \sim 0.1$–10 Hz. Owing to its sensitivity range, DECIGO would be able to observe inspiral sources that have advanced beyond the frequency band of the low frequency space-based GW detectors like eLISA, but which have not yet entered the ground detector band. eLISA is a space-based mission that is derived from the Laser Interferometer Space Antenna (LISA) proposal, with a slightly lowered design sensitivity. This mission is targeted towards GWs in the low-frequency band: 0.1 mHz to 1 Hz. The DECIGO

noise curve used in this work is adopted from Yagi and Seto [28]:

$$S_n(f) = 6.53 \times 10^{-49} \left[1 + \left(\frac{f}{f_p}\right)^2\right] + 4.45 \times 10^{-51} \left(\frac{f}{1\,\mathrm{Hz}}\right)^{-4} \frac{1}{1 + \left(\frac{f}{f_p}\right)^2} + 4.94 \times 10^{-52} \left(\frac{f}{1\,\mathrm{Hz}}\right)^{-4} \mathrm{Hz}^{-1}, \quad (9)$$

where $f_p = 7.36\,\mathrm{Hz}$. The first term in the expression represents the shot noise. The second and third terms represent the radiation pressure noise and the acceleration noise, respectively. The DECIGO band may be apt for the detection of GW emanating from the coalescences of intermediate-mass BH binaries.

2.3.2. *Future ground-based detectors*

– advanced LIGO: The advanced Laser Interferometer Gravitational-Wave Observatory (aLIGO) is taken as a representative of the second generation of ground-based detectors. The strain sensitivity of aLIGO is designed to be about a factor of 10 better than LIGO. aLIGO is expected to be able to observe NS binaries up to a distance of about 200 Mpc, which is around 15 times further than initial LIGO. The noise curve for the advanced LIGO detectors is adopted here from Keppel and Ajith [30]:

$$S_n(f) = 10^{-49} \left[\left(\frac{f}{f_0}\right)^{-4.14} - 5\left(\frac{f}{f_0}\right)^{-2} + 111\left(\frac{1 - \left(\frac{f}{f_0}\right)^2 + \left(\frac{f}{f_0}\right)^4/2}{1 + \left(\frac{f}{f_0}\right)^2/2}\right)\right] \mathrm{Hz}^{-1}. \quad (10)$$

Here $f_0 = 215\,\mathrm{Hz}$ is a scaling frequency [31]. Note that, even though some modified (estimated) noise curves are now available for the advanced LIGO detector, it suffices for our purpose to take the above analytical fit to the advanced LIGO noise curve. The detailed features of the noise curve are not very important here, since we are mainly interested in studying the synergy between the ground- and space-based telescopes.

– ET: The Einstein Telescope (ET) is a European Commission project that aims at developing a third-generation GW observatory. The higher sensitivity increases the number of events and the signal-to-noise ratio (SNR) of detected GWs for the same source, which would allow the extraction of more detailed information. The following noise curve is taken from Keppel and Ajith [30], and was obtained by assuming ET to be a single L-shaped interferometer with a 90° opening angle, for simplicity, and an arm length of 10 km. The predicted noise spectral density of such a configuration (ET-B) is given by:

$$S_n(f) = 10^{-50} \left[2.39 \times 10^{-27} \left(\frac{f}{f_0}\right)^{-15.64} + 0.349 \left(\frac{f}{f_0}\right)^{-2.145} + 1.76 \left(\frac{f}{f_0}\right)^{-0.12} + 0.409 \left(\frac{f}{f_0}\right)^{1.1}\right]^2 \mathrm{Hz}^{-1}, \quad (11)$$

where $f_0 = 100\,\mathrm{Hz}$. The noise curves for the various detectors are plotted in Fig. 1. In the following section we briefly discuss the error estimation scheme we use in this work.

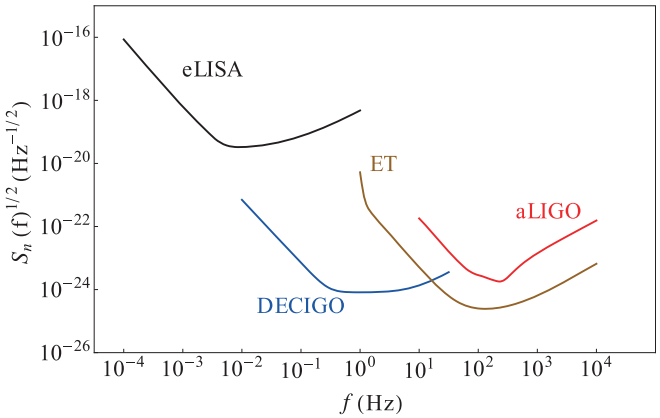

Fig. 1. Noise spectra for different GW detectors.

2.4. Likelihood function and Fisher matrix

In this subsection we give a brief overview of the Fisher matrix (FM) method used for computing errors in the estimation of parameters. For excellent reviews on this topic, we refer readers to Refs. [22,32,33]. We assume that the GW signal depends on the parameter vector $\boldsymbol{\theta}$. In the case of the PN waveform, $\boldsymbol{\theta} = \{\log \mathcal{M}, \nu, t_c, \phi_c\}$, whereas, in the case of the ppE framework, $\boldsymbol{\theta} = \{\log \mathcal{M}, \nu, t_c, \phi_c, \beta_i\}$ (in this work the ppE parameter c_i is fixed to zero for all i). The noise-weighted inner product for two signals $h_1(t)$ and $h_2(t)$ is defined as:

$$(h_1, h_2) = 2\int_0^\infty \frac{\tilde{h}_1^*(f)\tilde{h}_2(f) + \tilde{h}_2^*(f)\tilde{h}_1(f)}{S_n(f)} df, \tag{12}$$

where $\tilde{h}_1(f)$ and $\tilde{h}_2(f)$ are the Fourier transforms of $h_1(t)$ and $h_2(t)$, respectively, "$*$" represents the complex conjugation, and the signals are weighted by the expected power spectral density of detector noise $S_n(f)$. The inner product (12) is defined so that the probability that the signal is characterized by the parameters $\boldsymbol{\theta}$ (assuming Gaussian noise) is given by

$$P(s|\boldsymbol{\theta}) \propto e^{-(s-h(\boldsymbol{\theta}),s-h(\boldsymbol{\theta}))/2}.$$

Hence, the inner product is similar to defining a chi-squared merit function. Given an output $s(t)$, the best-fit GW waveform $h(\boldsymbol{\theta})$ is obtained by minimizing this inner product [32]. For different realizations of noise, we may obtain slightly different values of the parameters, but for large signal-to-noise ratios they will all be centered around the correct values, say, $\bar{\boldsymbol{\theta}}$, with some spread $\Delta\boldsymbol{\theta}$. The estimated errors follow a Gaussian distribution given by:

$$P\left(\Delta\theta^i\right) \propto e^{-\Gamma_{ij}\Delta\theta^i\Delta\theta^j/2}. \tag{13}$$

Here we have assumed the summation convention, where repeated indices are summed over, and Γ_{ij} is the FM defined as [22]

$$\Gamma_{ij} \equiv \left(\frac{\partial h}{\partial\theta_i}, \frac{\partial h}{\partial\theta_j}\right). \tag{14}$$

In the FM formalism, the inverse of the FM gives the spread around the peak of the multidimensional probability distribution $P(\boldsymbol{\theta}|s)$, yielding the variance of the posterior probability distribution. This is true in the high-SNR limit (and uniform priors for parameters over the regions of interest), where the SNR is defined so as to characterize the strength of the signal in a detector. Whether

a signal can be detected or not depends on whether the detector response is greater than its intrinsic noise amplitude, and this is the idea behind the definition of SNR [34]:

$$\rho = \frac{S}{N} = (h, h)^{1/2}. \tag{15}$$

As mentioned earlier, in the strong signal limit, the inverse of the FM gives the covariance matrix $C = \Gamma^{-1}$ and, the root mean square error in the estimate of the parameters can be evaluated from the diagonal elements of this matrix:

$$\sqrt{\left\langle \left(\Delta\theta^i\right)^2 \right\rangle} = \sqrt{C^{ii}}. \tag{16}$$

The off-diagonal elements of C are estimates of the covariances between the parameters. The error estimates (to be obtained from proposed surveys) on potentially interesting physical parameters can also be forecast through full Markov chain Monte Carlo simulations (MCMC). These are usually computationally expensive when the dimensionality of the parameter space is large, and are also time consuming. The FM technique to obtain the error estimates is much simpler and faster. Although it is frequently used in the GW community to indicate the expected performance of future GW detectors, one should be cautious in its use. As pointed out by many authors, the FM formalism is limited to high-SNR cases, which are often not realized in practice. Cornish and Porter were the first to note the discrepancies between the FM and MCMC methods. They found that, although the FM approach yields good estimates for the angular resolution and distance uncertainties, it overestimates the errors in the component masses and the time of coalescence [35]. Rodriguez et al. also studied the inadequacies of the FM formalism, and obtained similar results. They found that the FM formalism can overestimate the uncertainty in parameter estimation in the case of binary BH systems [36]. Vallisneri discussed the "use and abuse" of the FM method, arguing that, even though the high-SNR results are legitimate, the problem lies in justifying whether the signals are strong enough to validate this limit. The author further emphasized the significance of the singular Fisher matrices (which often arise in estimation in problems with multidimensional parameter space) [33]. In another work, Vallisneri proposed a semi-analytical technique to map the sampling distribution of the maximum likelihood estimator. The maps can be used to study errors in the estimated parameters and can also be used as a consistency check on the FM predictions for low-SNR cases [37]. Cho et al. proposed an effective-Fisher matrix scheme for parameter estimation and showed good agreement between their formalism and the MCMC exploration [38,39]. In spite of its limitations, the FM method is the simplest way to infer parameter uncertainties from future surveys in a quick and inexpensive way. Since we are using very simplistic models for the compact binary systems, and our main aim is to study the synergy (or lack thereof) between ground–space detectors, we adopt the FM method for error estimations.

The FM formalism also makes it very easy to forecast the error estimates from joint measurements. To do this, one merely needs to add the Fisher matrices of the individual measurements, $\Gamma_{\rm Combined} = \Gamma_1 + \Gamma_2$. This is because the joint probability distribution for the two observations, $P(s|\boldsymbol{\theta})$, is given by the product of those obtained from the respective detectors. Then we invert the summed matrix to find the covariance matrix for the combined measurement, and the corresponding error estimate is given as

$$C_{\rm Combined} = \Gamma^{-1}_{\rm Combined}, \tag{17}$$

$$\Delta\theta^i_{\rm Combined} = \sqrt{C^{ii}_{\rm Combined}}. \tag{18}$$

Table 1. Time taken for the GW signal from a binary system to sweep the frequency range $f_{\rm low}$–$f_{\rm LSO}$ (1 year $\approx 3 \times 10^7$ seconds).

Binary mass	$f_{\rm initial}$ (Hz)	$f_{\rm final}$ (Hz)	time (seconds)
$1.4\,M_\odot + 10\,M_\odot$	0.1	10	5×10^7
$1.4\,M_\odot + 10\,M_\odot$	10	387 $(f_{\rm LSO})$	225
$1.4\,M_\odot + 100\,M_\odot$	0.1	10	1×10^7
$1.4\,M_\odot + 100\,M_\odot$	10	43 $(f_{\rm LSO})$	46

2.5. Studying the change in estimates by varying the design sensitivity of DECIGO

Currently the roadmap to the proposed launch of DECIGO includes an observational mission at a smaller scale, called pre-DECIGO. pre-DECIGO will provide key insights about the technical feasibility of the final mission. The sensitivity of pre-DECIGO is still to be decided depending on various aspects, including the scientific gain. So in addition to assuming the noise sensitivity as given in Eq. (9), we also study the synergy effect by varying the sensitivities of DECIGO, assuming pre-DECIGO. Here, for brevity, we simply call it DECIGO. In both better and worse directions (higher and lower sensitivities), the detector sensitivity is changed by scaling the fiducial noise curve uniformly over all frequencies. Namely, the scaled DECIGO noise curves are obtained as

$$S_n(f)^{\rm scaled} = \mathcal{K} S_n(f)^{\rm DECIGO}, \tag{19}$$

with a constant $\mathcal{K}$. While reporting the SNRs in the results, we only present the SNRs for the original (estimated) design sensitivities. Obtaining the SNRs for the scaled DECIGO is straightforward. Note that the SNR also scales according to the distance to the source. The SNRs reported in the tables in this paper are just reference values for our choice of fiducial source distance (200 Mpc).

2.5.1. Frequency cutoff

Here we discuss our choice of the frequency cutoff for the integral in Eq. (14). We fix $f = 0.1$ Hz and $f = 1$ Hz as the lower-frequency limit for DECIGO and ET, respectively. For advanced LIGO, it is set at 10 Hz. Future space-based detectors will have good sensitivity at frequencies even below this cutoff, but the evolution of the binary coalescence is really slow at lower frequencies. As we are interested in the synergy effect, binaries at such low frequencies are irrelevant for the current study. In Table 1, we give some indicative times that a GW signal from a binary may take to sweep between two frequencies, $f_{\rm initial}$ and $f_{\rm final}$. Here $f_{\rm LSO}$ is the frequency corresponding to the last stable orbit (roughly where the inspiral ends) given by $f_{\rm LSO} = c^3/\left(6^{3/2}\pi G M\right)$ in the limit of the large mass ratio. Note that the time taken from $f_{\rm LSO}$ to merger is negligible compared to the time taken to go from some representative lower frequency $f_{\rm initial}$ to $f_{\rm LSO}$. For the mass configurations that we have considered in this work, it will take a few years or more for the binaries to span the lower (10^{-3}–0.1 Hz) frequency range. The evolution is much faster in the mid–high-frequency range and we can observe the same events in both space- and ground-based detectors in an observation span of about one year.

Note that this study depends on being able to identify the same GW event in both the space- and ground-based measurements. This would be possible through the comparison of the approximate binary parameters (and approximate directions) identified in both measurements. Performing a correlation analysis for estimating the parameters of a coalescence event observed in the space detector with data that spans about a year (Table 1) would be computationally very challenging. However, when this signal enters the sensitivity band of the ground detector, matched filtering can be done

relatively easily since the number of cycles in the ground detector band is far less than the space detector. This will inform us as to which parameter regions should be searched in finer detail, which is another synergy effect. Once we know where the signal lies in the parameter space, performing optimal matched filtering with the space detector measurements will be computationally less expensive. This is the reason why we think it is reasonable to assume that the data observed both by ground and space detectors can be identified even if there is a time lag between the two observations.

3. Results

In this section we explore the expected errors in the parameter estimation when we combine outputs of ground- and space-based detectors. We discuss results for the various parameters in the PN and the ppE waveforms for coalescing binary systems. As mentioned earlier, we consider two NS–BH binary systems: a $1.4\,M_\odot + 10\,M_\odot$ binary and a $1.4\,M_\odot + 100\,M_\odot$ binary, at a distance of 200 Mpc. We report the error estimates and the SNRs in the tables in the appendix.

We further analyze the variation in the error estimates on the parameters with the variation of the DECIGO sensitivity according to Eq. (19). As a reference, we introduce a quantity $\Delta\theta'$ for a parameter θ, which corresponds to the error estimate from the combined measurement if that single parameter was being estimated (Eq. (20)). In such a case, the joint probability for the combined estimate of some parameter, say, θ, is given by

$$\begin{aligned} P(\theta) &\propto e^{-(\theta-\bar{\theta}_1)^2/(2(\Delta\theta_1)^2)} \times e^{-(\theta-\bar{\theta}_2)^2/(2(\Delta\theta_2)^2)} \\ &= e^{-(\theta-\bar{\theta})^2/(2(\Delta\theta')^2)}, \end{aligned}$$

where $\bar{\theta}_1$ and $\bar{\theta}_2$ are the mean (the best-fit estimates) obtained for the parameter θ from the two measurements and $\Delta\theta_1$ and $\Delta\theta_2$ are the error estimates from the first and second measurements, respectively. $\bar{\theta}$ is the estimate from the combined measurement and $\Delta\theta'$ is the combined error estimate:

$$\Delta\theta' = \frac{\Delta\theta_1\,\Delta\theta_2}{\sqrt{\Delta\theta_1^2 + \Delta\theta_2^2}}. \tag{20}$$

These reference values are, of course, different from the correct estimate $\Delta\theta^i_{\rm Combined} = \sqrt{C^{ii}_{\rm Combined}}$ based on $C_{\rm Combined}$ given in Eq. (18). The correct estimates of errors normalized by these reference values are shown in Figs. 2 and 5. Plotting the ratio $\Delta\theta^i_{\rm Combined}/\Delta\theta'^i$ clarifies the synergy effect (and where it occurs in the pre-DECIGO range) visually. We expect that for very low DECIGO sensitivities the error estimate will be dominated by ET, while for very high DECIGO sensitivities they will be dominated by DECIGO. In both of these limiting cases, we do not expect a lot of gain in combining the space–ground measurements. Note that, in all the figures shown, the curves are obtained by varying the DECIGO sensitivity. In Figs. 2–4, 6, the horizontal axis is $\Delta\boldsymbol{\theta}_{\rm DECIGO}/\Delta\boldsymbol{\theta}_{\rm ET}$, which means that we vary the noise curve of DECIGO to obtain multiple values of $\Delta\boldsymbol{\theta}_{\rm DECIGO}$, which are then divided by $\Delta\boldsymbol{\theta}_{\rm ET}$ (which is a constant). Such a ratio is defined since we expect the synergy to take effect when this ratio is $\sim$1. In Figs. 5 and 7 we again obtain the curves by varying the DECIGO sensitivity, but in these cases the horizontal axis is $S_n(f)^{\rm scaled}/S_n(f)^{\rm DECIGO}$, where $S_n(f)^{\rm scaled}$ is as defined in Eq. (19), and $S_n(f)^{\rm DECIGO}$ is the original DECIGO noise curve as in Eq. (9). Such a ratio is defined to see at what sensitivities of (scaled) DECIGO, we get most synergy with ET. Note that defining these two ratios ($\Delta\boldsymbol{\theta}_{\rm DECIGO}/\Delta\boldsymbol{\theta}_{\rm ET}$ or $S_n(f)^{\rm scaled}/S_n(f)^{\rm DECIGO}$) for plotting purposes is just to visualize the same synergy effect in different ways.

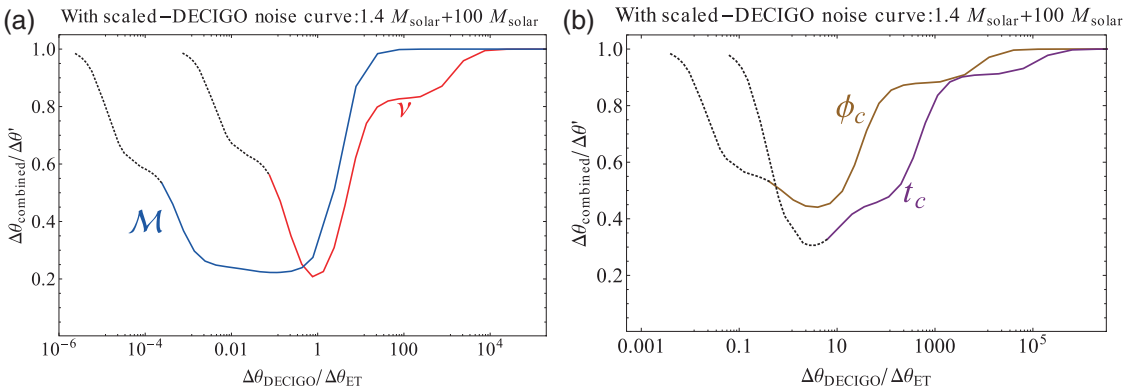

Fig. 2. Variation in the (scaled) error estimates of the chirp mass and the symmetric mass ratio (a) and the time and phase at coalescence (b), obtained by varying DECIGO sensitivities. $\Delta\theta_{\rm Combined}$ ($\theta = \mathcal{M}/\nu/t_c/p_c$) is obtained as explained in Sect. 2.4, and $\Delta\theta'$ is as given in Eq. (20). The ratio is plotted against $\Delta\theta_{\rm DECIGO}/\Delta\theta_{\rm ET}$, instead of $\Delta\theta_{\rm DECIGO}$ (which varies with varying DECIGO sensitivities) to see how the scaled-DECIGO estimate compares with $\Delta\theta_{\rm ET}$ when maximum synergy is obtained between the two measurements. The dotted curves correspond to better sensitivity than DECIGO. Note that the plateau region for the chirp mass in (a) does not imply that the error estimates remain constant with varying DECIGO sensitivity. The quantity that is plotted on the y-axis is not $\Delta\mathcal{M}_{\rm Combined}$, which can be seen in the following figure, Fig. 3, but a ratio that remains nearly the same while changing the DECIGO sensitivity in that range, owing to the fact that both its numerator and denominator scale by almost the same amount.

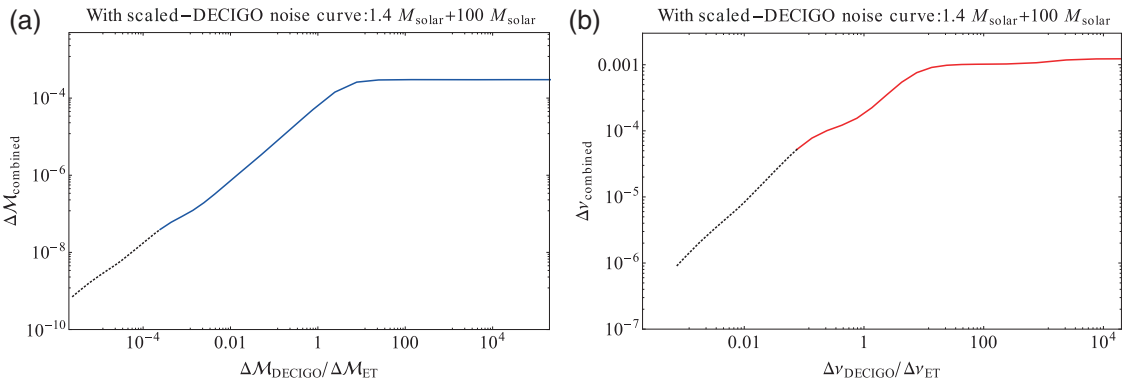

Fig. 3. Variation in the error estimates on the chirp mass (a) and the symmetric mass ratio (b) with varying DECIGO sensitivities. Estimates are plotted against $\Delta\theta_{\rm DECIGO}/\Delta\theta_{\rm ET}$ to see how the scaled-DECIGO estimate compares with $\Delta\theta_{\rm ET}$ when maximum synergy is obtained between the two measurements.

Note that if there is no degeneracy between the parameters, the ratio $\Delta\theta^i_{\rm Combined}/\Delta\theta'^i$ is equal to unity. Hence the dip shown in the plots, e.g., in Fig. 2, characterizes the merit of obtaining better estimates on some parameters from the paired detectors. We discuss this effect in more detail in the following section.

3.1. Error estimation: PN expansion

Here we present the error estimates on the chirp mass, the symmetric mass ratio, and the phase and time at coalescence using the method described in the previous section. In Tables A1 and A2 we report these errors for both independent and combined measurements. We note that there is some gain in combining space–ground measurements for all parameters:

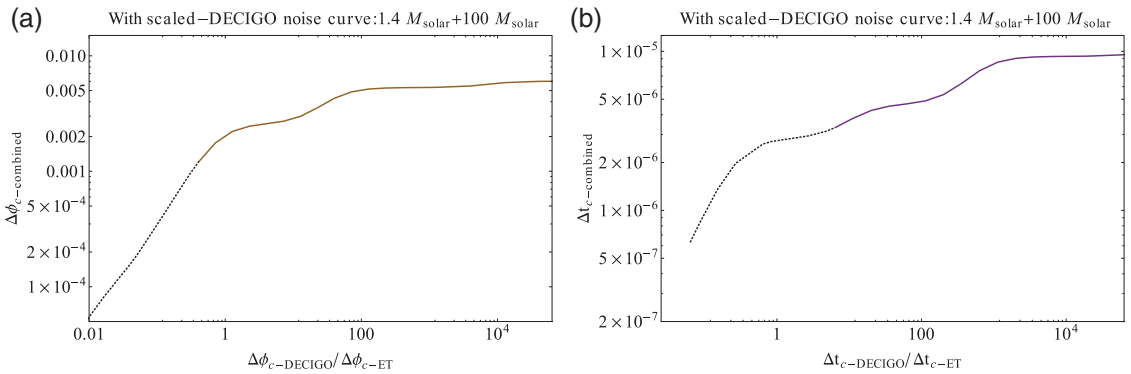

Fig. 4. Variation in the error estimates on the phase at coalescence (a) and the time of coalescence (b) with varying DECIGO sensitivities. Estimates are plotted against $\Delta\theta_{\rm DECIGO}/\Delta\theta_{\rm ET}$ to see how the scaled-DECIGO estimate compares with $\Delta\theta_{\rm ET}$ when maximum synergy is obtained between the two measurements.

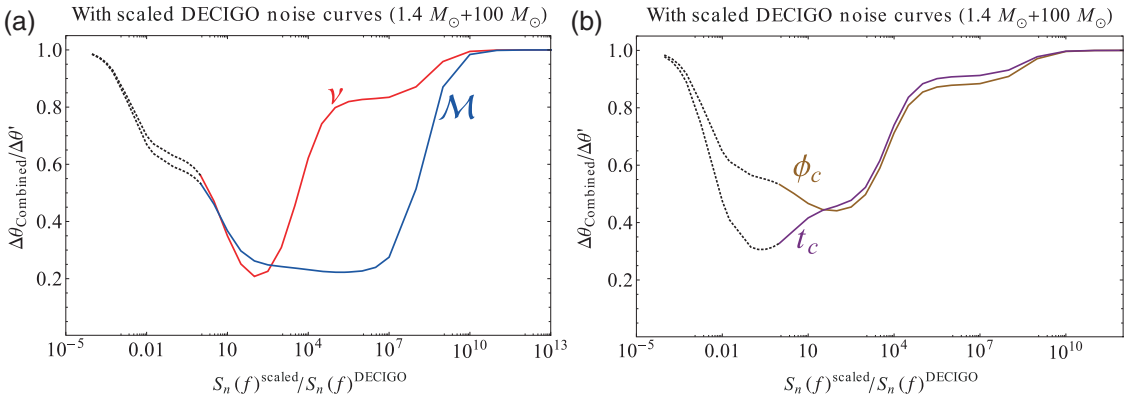

Fig. 5. Variation in the (scaled) error estimates of the chirp mass and the symmetric mass ratio (a) and the time and phase at coalescence (b), obtained by varying DECIGO sensitivities. The y-axis is the same as in Fig. 2, but the horizontal axis is chosen to see how the scaled-DECIGO sensitivity compares with DECIGO sensitivity when maximum synergy is obtained between the two measurements. One can see that synergy is obtained before reaching the DECIGO sensitivity (in the pre-DECIGO phase). The two saturations in the plot that are due to the worst DECIGO sensitivity (extreme right) and post-DECIGO sensitivities (extreme left) demonstrate ET dominance and DECIGO dominance in the error budget, respectively.

– In the case of the chirp mass, we find that one of the GW detectors dominates the error estimate and, for the time of coalescence, maximum gain is obtained for the detector pair ET–DECIGO.
– For the symmetric mass ratio and the phase of coalescence, there is no substantial gain in combining the space–ground measurements since one of the detectors always dominates the error budget.

Similarly, from our study on the synergy between (scaled) DECIGO and ET, we can infer the following about the PN template parameters:

– For the chirp mass, there is a wide range of sensitivities in the pre-DECIGO era (sensitivities that are 10–10^7 orders of magnitude worse than DECIGO) where there is substantial gain in combining the space–ground measurements.
– For the symmetric mass ratio and the phase at coalescence, maximum gain is obtained when the pre-DECIGO sensitivity is almost 10^2 orders of magnitude worse than DECIGO.

– For the time at coalescence, maximum gain is achieved in the post-DECIGO phase where the sensitivity is almost an order of magnitude better than DECIGO.

The results are shown in Figs. 2–5. In Figs. 2 and 5 we plot the normalized error estimates to clearly see the synergy effect, and we can see that at both extremes (when one of the detectors dominates the error budget), the normalized error saturates, and in the mid-range there is a dip. In Figs. 3 and 4 we plot the (unnormalized) errors on the parameters. When we look at these plots from left to right, it is evident that the total error budget is initially dominated by the (post-) DECIGO sensitivity as the curve rises monotonically with decreasing DECIGO sensitivity, after which the slope fluctuates until it eventually saturates to ET sensitivity.

As mentioned earlier, there is degeneracy between the estimates of the the chirp mass $\mathcal{M}$ and the symmetric mass ratio ν. This can be seen in Fig. 5. One can see here that there is a wide range of DECIGO sensitivities, in which the ratio of $\Delta\mathcal{M}_{\rm Combined}/\Delta\mathcal{M}'$ does not change appreciably (note that the error estimate of $\mathcal{M}_{\rm Combined}$ does change when we change DECIGO sensitivity, as can be seen in the left-hand panel of Fig. 3). If we trace the red curve (for the symmetric mass ratio ν) from right to left for the same range of DECIGO sensitivities, we find that ν is not well determined by DECIGO for most of this range $\left(S_n(f)^{\rm scaled}/S_n(f)^{\rm DECIGO} \approx 10^7 \rightarrow S_n(f)^{\rm scaled}/S_n(f)^{\rm DECIGO} \approx 10^4\right)$. Maximum synergy between the detectors in the estimation of ν is obtained towards the end of this slowly varying flat valley of the chirp mass. Namely, throughout the flat valley, $\mathcal{M}$ is mostly determined by DECIGO and ν by ET. The resolution of the degeneracy between $\mathcal{M}$ and ν by combining the two detectors is the main origin of the synergy effect. When the flat valley ends, DECIGO starts having better sensitivity towards ν than ET and can determine it by itself. Hence the merit of adding the ET measurements is reduced significantly and eventually we reach saturation again.

3.2. *Error estimation: ppE expansion*

We present the results of the analysis for 1PN, 2PN, and 3PN modifications to GR in this section. Here 1PN, 2PN, and 3PN modifications mean that we fix $b = -1, -1/3$, and $1/3$ in Eq. (7), respectively. The 1PN correction corresponds to the traditional massive graviton theory [13], and the 2PN correction corresponds to quadratic curvature theory [13]. With distance fixed at 200 Mpc, the results are shown in Tables A3 and A4 for 1PN, Tables A5 and A6 for 2PN, and Tables A7 and A8 for 3PN. In all cases, we find some gain to the constraint on these modifications to GR when combining the measurements of the space- and ground-based detectors.

In order to clarify the synergy effect, we present plots similar to Figs. 2 and 5 for the parameters β_i that characterize the modification to GR. As before, we plot the error estimates $\Delta\beta$ based on Eq. (18), relative to the reference value $\Delta\beta'$ defined by Eq. (20), for combined measurements from scaled DECIGO and ET (Fig. 6). As expected, for very low DECIGO sensitivities the error estimates are dominated by ET, while for very high DECIGO sensitivities they are dominated by DECIGO. In both limiting cases we do not find any merit of combining the space–ground measurements. However, in the middle frequency range there is a sweet spot where the gain becomes significantly large.

As before, the horizontal axis in Fig. 6 is $\Delta\beta_{\rm DECIGO}/\Delta\beta_{\rm ET}$. For all the different PN-order modifications (1PN, 2PN, and 3PN), the sweet spot appears around $\Delta\beta_{\rm DECIGO}/\Delta\beta_{\rm ET} \approx 1$, where both detectors equally contribute to constrain the parameter β. In Fig. 6b we show the variation of $\Delta\beta_{\rm Combined}$ with $\Delta\beta_{\rm DECIGO}$, which is obtained from the varying DECIGO sensitivity (and further normalized by $\Delta\beta_{\rm ET}$). In the region with $\Delta\beta_{\rm DECIGO}/\Delta\beta_{\rm ET} \ll 1$, the error estimates are dominated

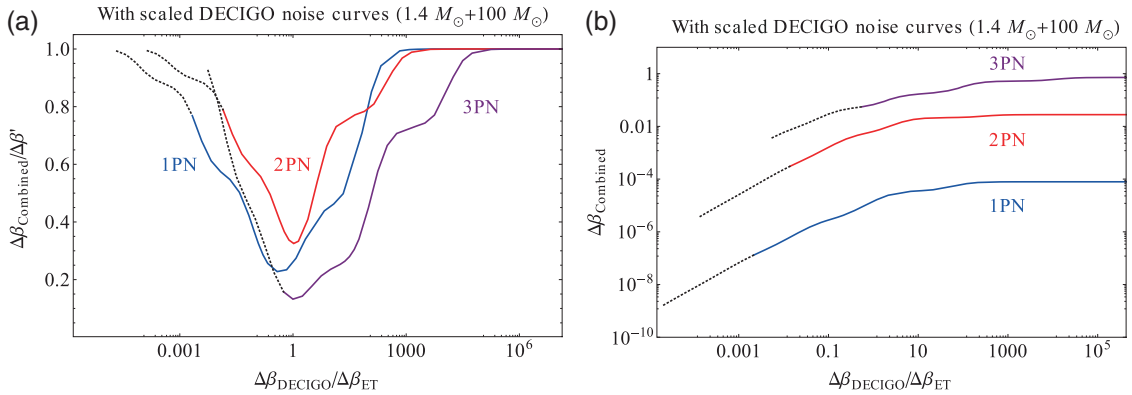

Fig. 6. Variation in the (normalized) error estimates on the GR modification parameter at different PN orders. $\Delta\beta_{\rm Combined}$ is obtained as explained in Sect. 2.4, and $\Delta\beta'$ is as given in Eq. (20). The dotted part corresponds to the noise curves with better sensitivity than DECIGO.

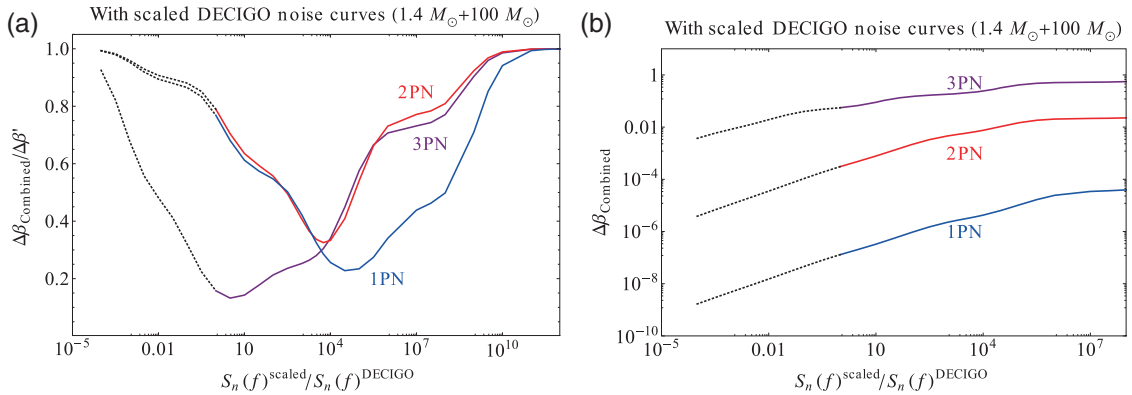

Fig. 7. Variation in the error estimates on the GR modification parameter with varying pre-DECIGO sensitivity. $\Delta\beta_{\rm Combined}$ is obtained as explained in Sect. 2.4, and $\Delta\beta'$ is as given in Eq. (20). The dotted curves correspond to better sensitivity than DECIGO.

by the DECIGO sensitivity, and hence they show a monotonic dependence. In the region with $\Delta\beta_{\rm DECIGO}/\Delta\beta_{\rm ET} \gg 1$, the error estimates are dominated by the ET sensitivity, and hence the curves become almost flat. At around $\Delta\beta_{\rm DECIGO}/\Delta\beta_{\rm ET} \approx 1$, the slope of the curves changes. This change is not monotonic, and corresponds to the sweet spot in Fig. 6a, where the true joint estimates are better than the reference estimates given by $\Delta\beta'$.

We also present these error estimates as functions of the sensitivity level of scaled DECIGO in Fig. 7. The higher-order PN terms tend to be better determined by the ground-based detectors, which have better sensitivities at higher frequencies. Hence, for higher PN-order terms, the synergy is maximum (i.e., the space and ground detectors contribute almost equally) for higher sensitivity of scaled DECIGO. The positions of the sweet spots in Fig. 5 can be understood in the same way by noticing that the leading-order frequency dependences of the chirp mass, the symmetric mass ratio, and the phase and time at coalescence are 0PN, 1PN, 2.5PN, and 4PN, respectively.

4. Conclusions

In this paper we have assessed the expected synergy effects between ground- and space-based detectors in the determination of binary coalescence parameters. For this we study the estimated errors

on the parameters of these systems. Note that, although we have considered only NS–BH systems, a similar study of binary black hole (BH–BH) systems can also be carried out. Owing to their larger masses, the lower-frequency cutoff in those cases can be further lowered. For example, for a $100\,M_\odot + 100\,M_\odot$, the lower-frequency cutoff can be set at 0.01 Hz instead of 0.1 Hz.

Our aim was to demonstrate that the advantages of having a GW antenna that is sensitive at low frequencies are larger than we naively expect. Larger gain in the error estimate of the binary parameters is obtained when the constraints from individual ground or space detectors are almost equal. In the case of the ppE parameters that characterize deviations from GR, some gain is always obtained irrespective of the level of sensitivity of the GW antenna. For lower PN-order corrections, some gain can be obtained even if the sensitivity of the space detector is degraded. The same argument also applies to the estimated errors in the extraction of binary parameters contained in the standard PN templates. In the present paper, neglecting the spins, we considered the chirp mass, the symmetric mass ratio, and the phase and time at coalescence, whose leading-order frequency dependences on the GW phase are 0PN, 1PN, 2.5PN, and 4PN, respectively. We found a sweet spot in the combined estimates of the chirp mass and the symmetric mass ratio in the pre-DECIGO phase (lower sensitivity than DECIGO). In these regions, the combined error estimates are better than the individual detector estimates. Substantial gain was also obtained in the joint measurement of the time and phase at coalescence. Here also the sweet spot was in the pre-DECIGO phase for the phase at coalescence, but for the time at coalescence, maximum gain was obtained with post-DECIGO sensitivity. As expected, for higher PN-order parameters, synergy is obtained at higher sensitivities of the space-borne GW detector. Note here that our results should be considered only as qualitative indications. To understand the features of the posterior distribution of the parameter space it is better to do a thorough exploration using some sampling scheme like MCMC.

In this work we have restricted the analysis to only four parameters from the 9-parameter set that describes the GWs from spinless binary systems. We do this mainly for simplicity. The information about the location of the source as expected from space measurements is extremely important. We will consider a more detailed analysis including sky location etc. in our future work. We can expect some changes in our results since the sky position may have a correlation with the parameters that we studied in this work, but we think that it will not change the significance of the synergy effect.

The sensitivity of space-borne GW antennae such as pre-DECIGO, which is a precursor mission for DECIGO, is still to be determined by considering various aspects including the scientific gain. The study of the synergy effects reported in the present paper provides valuable information and can be taken into account in making such decisions. Detection of GW150914 has heralded an era of GW astronomy and we need to make such decisions in the near future.

Acknowledgements

This work was supported by a MEXT Grant-in-Aid for Scientific Research on Innovative Areas, "New Developments in Astrophysics Through Multi-Messenger Observations of Gravitational Wave Sources", Nos. 24103001 and 24103006. This work was also supported in part by a Grant-in-Aid for Scientific Research (B) No. 26287044 and 15H02087. R.N. acknowledges support under the CSIR-SRF scheme (Government of India), and thanks the Department of Physics, Kyoto University, where part of this work was done, for hospitality. R.N. also thanks Sukanta Bose and Anuradha Gupta for discussions and suggestions. S.J. acknowledges support from a grant under the ISRO-RESPOND program (ISRO/RES/2/384/2014-15).

Appendix

Table A1. Error estimates for PN waveform parameters for individual detector measurements of DECIGO (first two rows), aLIGO (middle two rows), and ET (bottom two rows). These are calculated for NS–BH binaries with masses $1.4\,M_\odot + 10\,M_\odot$ and $1.4\,M_\odot + 100\,M_\odot$, with the distance fixed at 200 Mpc. The SNRs are also reported.

Binary mass	Δt_c	$\Delta\phi_c$	$\Delta\mathcal{M}/\mathcal{M}(\%)$	$\Delta\nu/\nu(\%)$	SNR
$1.4\,M_\odot + 10\,M_\odot$	9.16×10^{-5}	9.70×10^{-4}	9.57×10^{-8}	2.60×10^{-4}	2.02×10^{3}
$1.4\,M_\odot + 100\,M_\odot$	6.52×10^{-5}	2.43×10^{-3}	7.36×10^{-8}	9.36×10^{-5}	4.43×10^{3}
$1.4\,M_\odot + 10\,M_\odot$	3.22×10^{-4}	3.26×10^{-1}	1.62×10^{-2}	4.52×10^{-1}	1.68×10^{1}
$1.4\,M_\odot + 100\,M_\odot$	2.09×10^{-4}	1.49×10^{-1}	3.43×10^{-2}	3.53×10^{-2}	3.69×10^{1}
$1.4\,M_\odot + 10\,M_\odot$	1.51×10^{-5}	1.64×10^{-2}	1.35×10^{-4}	1.31×10^{-2}	2.16×10^{2}
$1.4\,M_\odot + 100\,M_\odot$	1.02×10^{-5}	6.02×10^{-3}	3.00×10^{-4}	1.23×10^{-3}	4.75×10^{2}

Table A2. Error estimates for PN waveform parameters for combined detector measurements from ET + DECIGO (first two rows) and aLIGO + DECIGO (bottom two rows). These are calculated for NS–BH binaries with masses $1.4\,M_\odot + 10\,M_\odot$ and $1.4\,M_\odot + 100\,M_\odot$, with the distance fixed at 200 Mpc.

Binary mass	Δt_c	$\Delta\phi_c$	$\Delta\mathcal{M}/\mathcal{M}(\%)$	$\Delta\nu/\nu(\%)$	SNR
$1.4\,M_\odot + 10\,M_\odot$	6.04×10^{-6}	8.98×10^{-4}	9.15×10^{-8}	2.46×10^{-4}	2.03×10^{3}
$1.4\,M_\odot + 100\,M_\odot$	3.31×10^{-6}	1.20×10^{-3}	3.92×10^{-8}	5.24×10^{-5}	4.46×10^{3}
$1.4\,M_\odot + 10\,M_\odot$	4.95×10^{-5}	9.22×10^{-4}	9.28×10^{-8}	2.50×10^{-4}	2.02×10^{3}
$1.4\,M_\odot + 100\,M_\odot$	2.56×10^{-5}	1.56×10^{-3}	4.90×10^{-8}	6.52×10^{-5}	4.43×10^{3}

Table A3. Error estimates for ppE waveform parameters, when the modification to GR appears at the first PN order, for individual detector measurements of DECIGO (first two rows), aLIGO (middle two rows), and ET (bottom two rows). These are calculated for NS–BH binaries with masses $1.4\,M_\odot + 10\,M_\odot$ and $1.4\,M_\odot + 100\,M_\odot$, with the distance fixed at 200 Mpc.

Binary mass	Δt_c	$\Delta\phi_c$	$\Delta\mathcal{M}/\mathcal{M}(\%)$	$\Delta\nu/\nu(\%)$	$\Delta\beta$
$1.4\,M_\odot + 10\,M_\odot$	1.56×10^{-4}	9.37×10^{-3}	1.85×10^{-7}	9.78×10^{-4}	2.48×10^{-7}
$1.4\,M_\odot + 100\,M_\odot$	7.56×10^{-5}	3.55×10^{-3}	3.76×10^{-7}	2.03×10^{-4}	1.69×10^{-7}
$1.4\,M_\odot + 10\,M_\odot$	7.16×10^{-4}	7.09×10^{-1}	9.13×10^{-2}	2.33	8.48×10^{-3}
$1.4\,M_\odot + 100\,M_\odot$	7.18×10^{-4}	1.93	1.32×10^{-1}	1.16×10^{-1}	5.46×10^{-2}
$1.4\,M_\odot + 10\,M_\odot$	2.33×10^{-5}	1.75×10^{-2}	4.64×10^{-4}	4.44×10^{-2}	8.86×10^{-5}
$1.4\,M_\odot + 100\,M_\odot$	2.01×10^{-5}	3.42×10^{-2}	7.98×10^{-4}	3.36×10^{-3}	7.89×10^{-5}

Table A4. Error estimates for ppE waveform parameters, when the modification to GR appears at the first PN order, for combined detector measurements from ET + DECIGO (first two rows) and aLIGO + DECIGO (bottom two rows). These are calculated for NS–BH binaries with masses $1.4\,M_\odot + 100\,M_\odot$ with the distance fixed at 200 Mpc.

Binary mass	Δt_c	$\Delta\phi_c$	$\Delta\mathcal{M}/\mathcal{M}(\%)$	$\Delta\nu/\nu(\%)$	$\Delta\beta$
$1.4\,M_\odot + 10\,M_\odot$	7.43×10^{-6}	4.54×10^{-3}	1.33×10^{-7}	5.84×10^{-4}	1.26×10^{-7}
$1.4\,M_\odot + 100\,M_\odot$	3.87×10^{-6}	1.47×10^{-3}	2.53×10^{-7}	1.09×10^{-4}	1.30×10^{-7}
$1.4\,M_\odot + 10\,M_\odot$	5.71×10^{-5}	6.12×10^{-3}	1.55×10^{-7}	7.32×10^{-4}	1.67×10^{-7}
$1.4\,M_\odot + 100\,M_\odot$	2.67×10^{-5}	2.15×10^{-3}	3.09×10^{-7}	1.46×10^{-4}	1.51×10^{-7}

Table A5. Error estimates for ppE waveform parameters, when the modification to GR appears at the second PN order, for individual detector measurements of DECIGO (first two rows), aLIGO (middle two rows), and ET (bottom two rows). These are calculated for NS–BH binaries with masses $1.4\,M_\odot + 10\,M_\odot$ and $1.4\,M_\odot + 100\,M_\odot$, with the distance fixed at 200 Mpc.

Binary mass	Δt_c	$\Delta\phi_c$	$\Delta\mathcal{M}/\mathcal{M}(\%)$	$\Delta\nu/\nu(\%)$	$\Delta\beta$
$1.4\,M_\odot + 10\,M_\odot$	1.63×10^{-4}	1.27×10^{-2}	1.66×10^{-7}	5.62×10^{-4}	3.51×10^{-4}
$1.4\,M_\odot + 100\,M_\odot$	7.45×10^{-5}	2.53×10^{-3}	4.40×10^{-7}	3.57×10^{-4}	3.88×10^{-4}
$1.4\,M_\odot + 10\,M_\odot$	3.95×10^{-3}	8.21×10^{1}	7.15×10^{-2}	4.21×10^{1}	1.60×10^{1}
$1.4\,M_\odot + 100\,M_\odot$	1.18×10^{-3}	7.02	6.25×10^{-2}	3.19×10^{-1}	9.05×10^{-1}
$1.4\,M_\odot + 10\,M_\odot$	1.00×10^{-4}	1.90	1.21×10^{-3}	9.95×10^{-1}	3.72×10^{-1}
$1.4\,M_\odot + 100\,M_\odot$	4.42×10^{-5}	2.22×10^{-1}	4.08×10^{-4}	1.14×10^{-2}	2.78×10^{-2}

Table A6. Error estimates for ppE waveform parameters, when the modification to GR appears at the second PN order, for combined detector measurements from ET + DECIGO (first two rows) and aLIGO + DECIGO (bottom two rows). These are calculated for NS–BH binaries with masses $1.4\,M_\odot + 100\,M_\odot$ with the distance fixed at 200 Mpc.

Binary mass	Δt_c	$\Delta\phi_c$	$\Delta\mathcal{M}/\mathcal{M}(\%)$	$\Delta\nu/\nu(\%)$	$\Delta\beta$
$1.4\,M_\odot + 10\,M_\odot$	7.64×10^{-6}	5.80×10^{-3}	1.21×10^{-7}	3.76×10^{-4}	1.66×10^{-4}
$1.4\,M_\odot + 100\,M_\odot$	4.15×10^{-6}	2.04×10^{-3}	3.13×10^{-7}	2.36×10^{-4}	3.06×10^{-4}
$1.4\,M_\odot + 10\,M_\odot$	5.77×10^{-5}	8.09×10^{-3}	1.41×10^{-7}	4.54×10^{-4}	2.28×10^{-4}
$1.4\,M_\odot + 100\,M_\odot$	2.67×10^{-5}	2.12×10^{-3}	3.74×10^{-7}	2.92×10^{-4}	3.52×10^{-4}

Table A7. Error estimates for ppE waveform parameters, when the modification to GR appears at the first PN order, for individual detector measurements of DECIGO (first two rows), aLIGO (middle two rows), and ET (bottom two rows). These are calculated for NS–BH binaries with masses $1.4\,M_\odot + 10\,M_\odot$ and $1.4\,M_\odot + 100\,M_\odot$, with the distance fixed at 200 Mpc.

Binary mass	Δt_c	$\Delta\phi_c$	$\Delta\mathcal{M}/\mathcal{M}(\%)$	$\Delta\nu/\nu(\%)$	$\Delta\beta$
$1.4\,M_\odot + 10\,M_\odot$	2.29×10^{-4}	6.43×10^{-3}	1.29×10^{-7}	3.86×10^{-4}	2.48×10^{-1}
$1.4\,M_\odot + 100\,M_\odot$	1.8×10^{-4}	3.24×10^{-2}	6.83×10^{-7}	6.75×10^{-4}	4.02×10^{-1}
$1.4\,M_\odot + 10\,M_\odot$	1.19×10^{-3}	7.69	2.93×10^{-2}	2.44	4.67×10^{1}
$1.4\,M_\odot + 100\,M_\odot$	2.09×10^{-4}	2.96	7.44×10^{-2}	3.79×10^{-1}	2.97×10^{1}
$1.4\,M_\odot + 10\,M_\odot$	4.80×10^{-5}	2.15×10^{-1}	1.52×10^{-4}	5.08×10^{-2}	1.38
$1.4\,M_\odot + 100\,M_\odot$	1.28×10^{-5}	7.81×10^{-2}	4.12×10^{-4}	7.53×10^{-3}	7.17×10^{-1}

Table A8. Error estimates for ppE waveform parameters, when the modification to GR appears at the third PN order, for combined detector measurements from ET + DECIGO (first two rows) and aLIGO + DECIGO (bottom two rows). These are calculated for NS–BH binaries with masses $1.4\,M_\odot + 100\,M_\odot$ with the distance fixed at 200 Mpc.

Binary mass	Δt_c	$\Delta\phi_c$	$\Delta\mathcal{M}/\mathcal{M}(\%)$	$\Delta\nu/\nu(\%)$	$\Delta\beta$
$1.4\,M_\odot + 10\,M_\odot$	1.15×10^{-5}	2.15×10^{-3}	9.73×10^{-8}	2.69×10^{-4}	6.62×10^{-2}
$1.4\,M_\odot + 100\,M_\odot$	7.10×10^{-6}	5.65×10^{-3}	1.30×10^{-7}	1.44×10^{-4}	5.53×10^{-2}
$1.4\,M_\odot + 10\,M_\odot$	6.72×10^{-5}	3.70×10^{-3}	1.13×10^{-7}	3.27×10^{-4}	1.3×10^{-1}
$1.4\,M_\odot + 100\,M_\odot$	4.31×10^{-5}	1.77×10^{-2}	3.87×10^{-7}	3.94×10^{-4}	2.00×10^{-1}

References

[1] B. P. Abbott et al., Phys. Rev. Lett. **116**, 061102 (2016).
[2] C. M. Will, Living. Rev. Relativ. **9**, 3 (2006).
[3] R. Narayan and J. E. McClintock, in *General Relativity and Gravitation: A Centennial Perspective*, eds. A. Ashtekar, B. Berger, J. Isenberg, and M. A. H. MacCallum (Cambridge University Press, Cambridge, UK, 2013.
[4] B. Allen, [arXiv:gr-qc/9604033] [Search INSPIRE].
[5] K. Yagi, Int. J. Mod. Phys. D **22**, 1 (2013).
[6] C. M. Will and N. Yunes, Classical Quantum Gravity **21**, 4367 (2004).
[7] N. Yunes and X. Siemens, Living. Rev. Relativ. **16**, 9 (2013).
[8] C. M. Will, Phys. Rev. D **50**, 6058 (1994).
[9] E. Berti, A. Buonanno, and C. M. Will, Phys. Rev. D **71**, 084025 (2005).
[10] C. K. Mishra et al., Phys. Rev. D **82**, 064010 (2010).
[11] K. G. Arun et al., Phys. Rev. D **74**, 024006 (2006).
[12] N. Yunes and F. Pretorius, Phys. Rev. D **80**, 122003 (2009).
[13] N. Cornish et al., Phys. Rev. D **84**, 062003 (2011).
[14] K. Yagi and T. Tanaka, Phys. Rev. D **81**, 064008 (2010).
[15] The LIGO Scientific Collaboration, [arXiv:1602.03840 [gr-qc]] [Search INSPIRE].
[16] L. Blanchet, Living. Rev. Relativ. **17**, 2 (2014).
[17] L. Blanchet, B. R. Iyer, and B. Joguet, Phys. Rev. D **65**, 064005 (2002).
[18] L. Blanchet et al., Phys. Rev. Lett. **93**, 091101 (2004).
[19] L. Blanchet et al., Classical Quantum Gravity **25**, 165003 (2008).
[20] T. Damour, P. Jaranowski, and G. Schafer, Phys. Rev. D **89**, 064058 (2014).
[21] B. S. Sathyaprakash and B. F. Schutz, Living. Rev. Relativ. **12**, 4 (2009).
[22] C. Cutler and E. E. Flanagan, Phys. Rev. D **49**, 6 (1994).
[23] A. Vecchio, Phys. Rev. D **70**, 042001 (2004).
[24] K. Nordtvedt, Phys. Rev. **169**, 1017 (1968).
[25] C. M. Will and K. Nordtvedt, Astrophys. J. **177**, 757 (1972).
[26] J. Crowder and N. J. Cornish, Phys. Rev. D **72**, 083005 (2005).
[27] N. Seto, S. Kawamura, and T. Nakamura, Phys. Rev. Lett. **87**, 221103 (2001).
[28] K. Yagi and N. Seto, Phys. Rev. D **83**, 044011 (2011).
[29] P. Amaro-Seoane et al., Classical Quantum Gravity **29**, 124016 (2012).
[30] D. Keppel and P. Ajith, Phys. Rev. D **82**, 122001 (2010).
[31] K. G. Arun et al., Phys. Rev. D **71**, 084008 (2005).
[32] L. S. Finn, Phys. Rev. D **46**, 12 (1992).
[33] M. Vallisneri, Phys. Rev. D **77**, 042001 (2008).
[34] M. Maggiore, *Gravitational Waves, Volume 1: Theory and Experiments* (Oxford University Press, Oxford, UK, 2008).
[35] N. J. Cornish and E. K. Porter, Classical Quantum Gravity **23**, S761 (2006).
[36] C. L. Rodriguez et al., Phys. Rev. D **88**, 084013 (2013).
[37] M. Vallisneri, Phys. Rev. Lett. **107**, 191104 (2011).
[38] H.-S. Cho et al., Phys. Rev. D **87**, 024004 (2013).
[39] H.-S. Cho and C.-H. Lee, Classical Quantum Gravity **31**, 235009 (2014).